

# A MUSE study of the inner bulge globular cluster Terzan 9: a fossil record in the Galaxy <sup>\*</sup>

H. Ernandes<sup>1,2,3</sup>, B. Dias<sup>4,5</sup>, B. Barbuy<sup>1</sup>, S. Kamann<sup>6</sup>, S. Ortolani<sup>7,8</sup>, E. Cantelli<sup>1</sup>, E. Bica<sup>9</sup>, and L. Rossi<sup>10</sup>

<sup>1</sup> Universidade de São Paulo, IAG, Rua do Matão 1226, Cidade Universitária, São Paulo 05508-900, Brazil

<sup>2</sup> UK Astronomy Technology Centre, Royal Observatory, Blackford Hill, Edinburgh, EH9 3HJ, UK

<sup>3</sup> IfA, University of Edinburgh, Royal Observatory, Blackford Hill, Edinburgh, EH9 3HJ, UK

<sup>4</sup> ESO, Alonso de Córdova 3107, Vitacura, Santiago de Chile, Chile

<sup>5</sup> Departamento de Física, Facultad de Ciencias Exactas, Universidad Andrés Bello, Av. Fernandez Concha 700, Las Condes, Santiago, Chile

<sup>6</sup> Astrophysics Research Institute, Liverpool John Moores University, 146 Brownlow Hill, Liverpool L3 5RF, UK

<sup>7</sup> Università di Padova, Dipartimento di Fisica e Astronomia, Vicolo dell'Osservatorio 3, 35122 Padova, Italy

<sup>8</sup> INAF-Osservatorio Astronomico di Padova, Vicolo dell'Osservatorio 5, 35122, Padova, Italy

<sup>9</sup> Universidade Federal do Rio Grande do Sul, Departamento de Astronomia, Av. Bento Gonçalves 9500, Rio Grande do Sul, Brasil

<sup>10</sup> Centre for Astrophysics and Supercomputing, Swinburne University of Technology, Hawthorn, VIC 3122, Australia

Received ; accepted

## ABSTRACT

**Context.** Moderately metal-poor inner bulge globular clusters are relics of a generation of long-lived stars that formed in the early Galaxy. Terzan 9, projected at 4°12 from the Galactic center, is among the most central globular clusters in the Milky Way, showing an orbit which remains confined to the inner 1 kpc.

**Aims.** Our aim is the derivation of the cluster's metallicity, together with an accurate measurement of the mean radial velocity. In the literature, metallicities in the range between  $-2.0 < [\text{Fe}/\text{H}] < -1.0$  have been estimated for Terzan 9 based on color-magnitude diagrams and CaII triplet (CaT) lines.

**Methods.** Given its compactness, Terzan 9 was observed using the Multi Unit Spectroscopic Explorer (MUSE) at the Very Large Telescope. The extraction of spectra from several hundreds of individual stars allowed us to derive their radial velocities, metallicities, and [Mg/Fe]. The spectra obtained with MUSE were analysed through full spectrum fitting using the ETOILE code.

**Results.** We obtained a mean metallicity of  $[\text{Fe}/\text{H}] \approx -1.10 \pm 0.15$ , a heliocentric radial velocity of  $v_r^h = 58.1 \pm 1.1 \text{ km s}^{-1}$ , and a magnesium-to-iron  $[\text{Mg}/\text{Fe}] = 0.27 \pm 0.03$ . The metallicity-derived character of Terzan 9 sets it among the family of the moderately metal-poor Blue Horizontal Branch clusters HP 1, NGC 6558, and NGC 6522.

**Key words.** stars: stellar parameters - Galaxy: bulge - globular clusters: individual (Terzan 9)

## 1. Introduction

Globular clusters in the central parts of the Galaxy are among the oldest extant stellar populations in the Milky Way (e.g. Barbuy et al. 2018a; Kunder et al. 2018). Terzan 9 is a very compact cluster located at 4°12 and 0.7 kpc (Bica et al. 2006) from the Galactic center, which is, thus, in the inner bulge volume, and it is among the globular clusters closest to the Galactic center. Terzan 9 appears to show a blue horizontal branch (BHB) in the ground-based color-magnitude diagrams (CMDs) by Ortolani et al. (1999). The clusters identified with a moderate metallicity and a BHB are very old as deduced from proper-motion cleaned color-magnitude diagrams (CMDs) for example for NGC 6522 and HP 1 (Kerber et al. 2018, 2019). A proper-motion cleaned CMD for Terzan 9 is presented in Rossi et al. (2015), with the cluster proper motions derived. Orbit cal-

culations by Pérez-Villegas et al. (2018) reveal that Terzan 9 remains confined within 1 kpc of the Galactic center with an orbit co-rotating with the bar, it has a bar shape in the (x - y) projection, and a boxy shape in (x - z), which indicates that these clusters are trapped by the bar. With absolute proper motions from Gaia DR2, a new orbital analysis was carried out (Pérez-Villegas et al. 2019) using a Monte Carlo method to take into account the effect of the uncertainties in the observational parameters. These calculations confirm that Terzan 9 belongs to the bulge globular cluster group and that most of its probable orbits follow the bar. Since the bulge clusters are typically old, they were probably formed early in the Galaxy and were later trapped by the bar (see also Renzini et al. 2018). As a matter of fact, the bar should have formed at about  $8 \pm 2$  Gyr ago, according to Buck et al. (2018).

A metallicity of  $[\text{Fe}/\text{H}] \sim -2.0$  is deduced by Ortolani et al. (1999) and  $[\text{Fe}/\text{H}] \sim -1.2$  by Valenti et al. (2007) from CMDs. Armandroff & Zinn (1988) obtained  $[\text{Fe}/\text{H}] = -0.99$  from measurements of CaT lines. Vásquez et al. (2018) (ESO proposal 089.D-0493) measured the CaT lines for

Send offprint requests to: H. Ernandes

<sup>\*</sup> Based on observations collected at the European Organisation for Astronomical Research in the Southern Hemisphere, Paranal, Chile, under ESO programme 097.D-0093

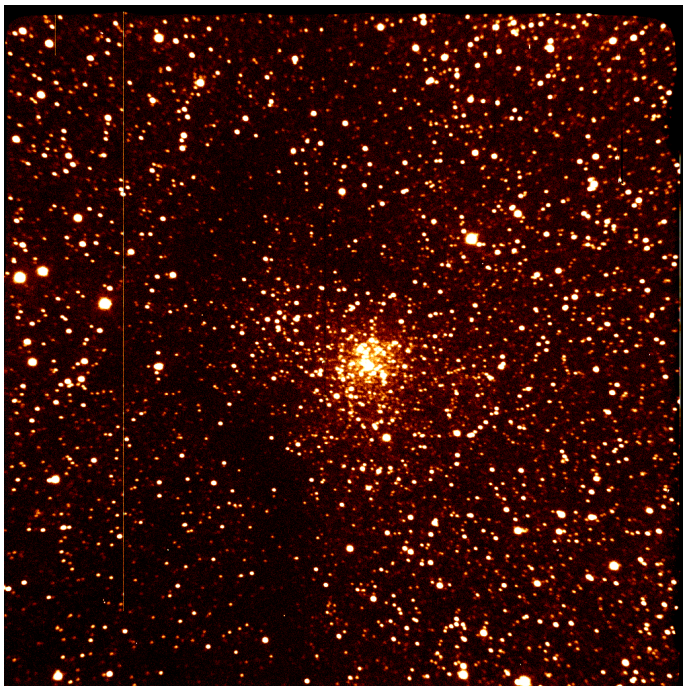


**Fig. 1.** Terzan 9: I image of Terzan 9 obtained at NTT in 2012, with seeing of 0.5 arcsec. Size is 2.2x2.2 arcmin<sup>2</sup>.

six stars and obtained  $[\text{Fe}/\text{H}] \sim -1.08, -1.21,$  and  $-1.16$  following calibrations from Dias et al. (2016), Saviane et al. (2012), and Vásquez et al. (2015), respectively. In the compilations by Harris (1996, Edition of 2010)<sup>1</sup> and Carretta et al. (2009), metallicities of  $[\text{Fe}/\text{H}] = -1.05$  and  $-2.07$  are respectively reported. Given that spectroscopic results are more reliable for metallicity derivations, it appears that a value of around  $[\text{Fe}/\text{H}] \sim -1.0$  should be preferred. The aim of this work is to obtain the metallicity derivation for Terzan 9, together with its radial velocity. The coordinates and typical photometric parameters for Terzan 9 are reported in Table 1.

**Table 1.** Terzan 9: data from literature. References: (1) Rossi et al. (2015), (2) Bica et al. (2006), (3) Ortolani et al. (1999), (4) Harris (1996, 2010 Edition).

RA J2000	18 01 38.80
DEC J2000	-26 50 23.0
$l(^{\circ})$	3.60
$b(^{\circ})$	-1.99
$R_{\text{Sun}}$ (kpc)	7.7 (1,2)
$R_{\text{GC}}$ (kpc)	0.7 (2)
$E(\text{B}-\text{V})$	1.87 (2)
$V_{\text{tip}}/V_{\text{HB}}$	17.5/20.35 (3)
$M_0$ $V,t$	-3.71 (4)

The ETOILE code (Katz et al. 2011, Dias et al. 2015) is used to derive the stellar parameters effective temperature, gravity, metallicity, and  $[\text{Mg}/\text{Fe}]$  ratio for each sample star. This code corrects for radial velocity, compares the observed spectra of a sample star to all spectra from a grid of spectra, and indicates which ones are the most similar. The procedure proved to work well, as demonstrated in Dias et



**Fig. 2.** Terzan 9: composed image in B, V and R, from 5 different pointings of Terzan 9 obtained with MUSE on Yepun in 2016. Size is 1.1x1.1 arcmin<sup>2</sup>, exposures with seeing from 0.51" to 1.01".

al. (2015, 2016), where the method is applied to 800 red giants in 51 globular clusters, observed with FORS2 at a similar resolution as MUSE, which is of the order of  $R \sim 2000$  at  $6000 \text{ \AA}$ .

In Sect. 2, we report our observations. In Sect. 3, the steps in data reduction are given. Extraction of stellar spectra is described in Sect. 4. The analysis with the derivation of stellar parameters and a discussion of results are presented in Sections 5 and 6. A summary is provided in Sect. 7.

## 2. Observations

Terzan 9 is faint and compact with a concentration factor of  $c = 2.50$  and core radius  $r_{\text{core}} = 0.03'$  (Harris 1996, updated in 2010), therefore the MUSE field of view (FoV) of  $1' \times 1'$  appears suitable to locate and identify a large number of member stars.

The input list of stars was created from a combination of the photometric observations of Ortolani et al. (1999) with the Danish telescope in 1998 and more recent observations with the NTT@ESO in 2012. The absolute calibration of the NTT 2012 data has been performed using our previous 1998 Danish data (Ortolani et al. 1999). About 800 stars in common between the Danish 1998 data and NTT 2012 have been matched and checked in order to transform the instrumental NTT magnitudes into the calibrated ones. Two almost linear relations in magnitude and colors have been found, with a residual slope, in a range within 0.01 mag, possibly due to minor linearity deviations mostly at magnitudes brighter than  $V < 16$ . A simple offset has been applied then to the instrumental magnitudes and colors. The formal error of the transformation in V and V-I is of about 0.025 magnitudes for both. The photometric error is dominated by linearity deviations at faint magnitudes. The

<sup>1</sup> [www.physic.mcmaster.ca/~harris/mwgc.dat](http://www.physic.mcmaster.ca/~harris/mwgc.dat)

V and I data were calibrated with the following conversion coefficients:

$$V_{\text{calibrated}} = V_{\text{NTT2012}} + 6.798 \pm 0.015$$

$$(V - I)_{\text{calibrated}} = (V - I)_{\text{NTT2012}} + 1.77 \pm 0.02$$

These two sets of data were combined in Rossi et al. (2015) and used for proper-motion decontamination, making use of the 14 yr time difference between the 1998 and 2012 observations to have an optimized selection of member stars. We transformed the original data given in pixels in X,Y into right ascension and declination (RA,DEC) based on the NTT 2012 image. The final coordinates are established by matching stars in common with the Gaia Data Release 2 (Gaia Collaboration 2018). The list of stars with their coordinates, along with their V and V-I, are reported in Table A.1. In Fig. 1, we show an I image of Terzan 9 obtained at the NTT in 2012, with an excellent seeing of 0.5".

The observations of the Terzan 9 field were conducted with the MUSE instrument installed on the UT4 Yepun unit of the Very Large Telescope (VLT), with the Wide Field Mode, no-AO, standard coverage (nominal mode WFM-NOAO-N). The FOV of MUSE in the Wide Field mode is 1'x1' per exposure. The total observing time was 5 hours including overheads, that were distributed along 5 observation blocks with 3 exposures (one in the central field and 2 offsets) of 948 seconds each. Besides a rotation of 90°, as recommended, and offsets of < 2 s in RA and of up to 18 s in DEC were applied. Detailed information about each exposure is given in Table 2. The MUSE datacubes were convolved with the transmission curves of the filters Red, Green and Blue, resulting in three images. The color composite image in B ( 4800 Å), V ( 5477 Å), and R ( 6349 Å). We note the Johnson-Cousins B filter overlaps only 22.77% of the MUSE wavelength coverage of 4800-9300 Å. That is the reason why the B in the color composing image, Fig. 2 is centered in 4800 Å instead of 4353 Å.

### 3. Data reduction

#### 3.1. Individual exposure reduction and sky subtraction

The individual exposures were reduced using the MUSE instrument pipeline v2.0.1 under the Reflex environment.

Since the field is highly crowded and reddened due to its location at low latitudes in the Galactic bulge, the sky subtraction must be carefully conducted. The MUSE pipeline gives the choice of the fraction of the FOV to be considered as sky. After some tests, we chose 6% based on the generated mask area, zones affected by sky contamination on the stellar spectra, and sky spectra comparisons assuming different fractions. For fractions much higher than 6%, the sky spectrum shows absorption lines of unresolved faint stars at redder wavelengths. For fractions much below 6% the final sky spectrum is not representative of the whole FOV, which implies that some sky-subtracted stellar spectra still show some sky emission lines.

The subtraction method used is simple, demonstrating a slight improvement in the signal-to-noise (S/N). Figures 3 (full wavelength range) and 4 (zoom on the bluest range) show the effect of sky subtraction. The faint sources are

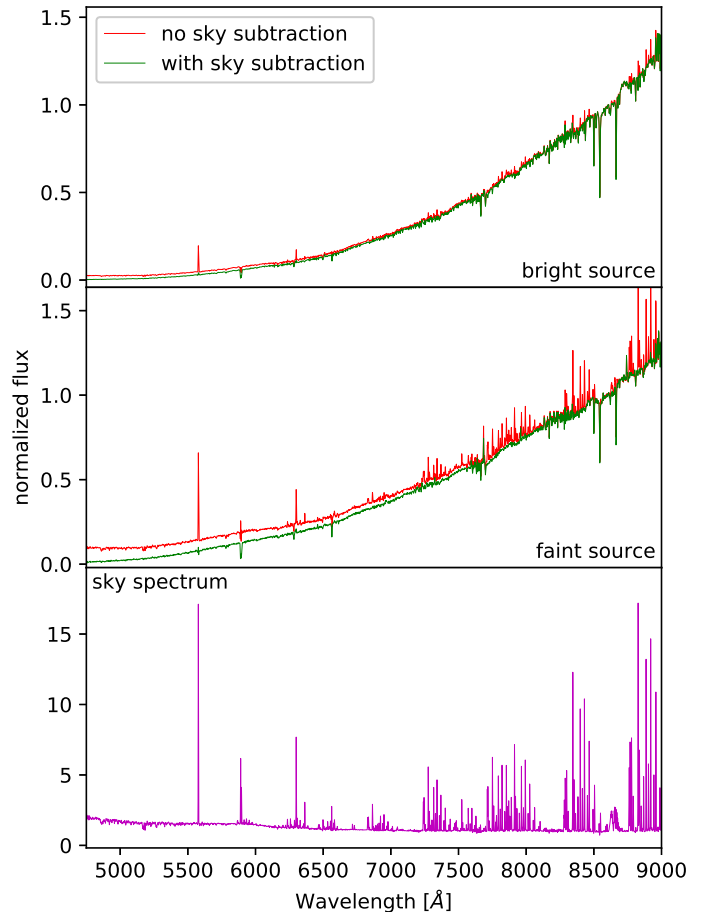


**Fig. 3.** Comparison between sky contribution to bright and faint stellar sources. Spectra are normalized to their flux at 8604 Å.

more affected by the sky than the bright ones because of their flux level being lower and closer to the sky level.

An example of spectra from different datacubes are shown in Fig. 6 for a sample star.

#### 3.2. Datacube combination

The combination of the exposures was done by observation block (OB) using the most recent version (v2.1.1) of the MUSE instrument pipeline available only in the Gasgano environment. Gasgano's interface allows for a quick assignment of frames to specific recipes and easy parameter manipulation, together with a processing request pool, so it is convenient for doing tests and requesting different datasets. We combined the three exposures of each OB to end up with five final cubes. The combination of all OBs was not done in the same way because they were observed in different conditions. The final stellar spectra correspond to the combination of the extracted 1D spectra of each star from the five cubes.

During the combination, several tests were carried out. The most influential parameter was the resampling method in building the combined cube. The MUSE pipeline default method is "drizzle" and comparisons between this method, along with other complex methods "renka" and "lanczos," were performed. The renka method showed the best spatial resolution and image coverage among the three. We performed some tests with the renka resample method to find

**Table 2.** Observation log.

cube name	date	exp. time	airm. start	airm. end	seeing start	seeing end	relative humidity
WFM_Ter9_OB1_exp1	2016-05-28T06:37:58	948	1.003	1.01	0.51	0.51	17.5
WFM_Ter9_OB1_exp2	2016-05-28T06:55:37	948	1.011	1.023	0.56	0.62	17.5
WFM_Ter9_OB1_exp3	2016-05-28T07:13:16	948	1.024	1.041	0.57	0.80	15.0
WFM_Ter9_OB2_exp1	2016-05-28T07:39:44	948	1.053	1.078	0.72	0.53	17.0
WFM_Ter9_OB2_exp2	2016-05-28T07:57:35	948	1.08	1.112	0.53	0.59	17.0
WFM_Ter9_OB2_exp3	2016-05-28T08:15:43	948	1.115	1.155	0.59	0.87	15.5
WFM_Ter9_OB3_exp1	2016-06-05T06:58:55	948	1.041	1.063	1.01	0.89	35.0
WFM_Ter9_OB3_exp2	2016-06-05T07:16:45	948	1.065	1.093	0.97	0.91	35.0
WFM_Ter9_OB3_exp3	2016-06-05T07:34:40	948	1.095	1.131	0.95	0.86	35.0
WFM_Ter9_OB4_exp1	2016-06-09T03:35:40	948	1.116	1.083	0.77	0.63	4.5
WFM_Ter9_OB4_exp2	2016-06-09T03:53:47	948	1.081	1.055	0.63	0.72	4.0
WFM_Ter9_OB4_exp3	2016-06-09T04:12:05	948	1.053	1.033	0.73	0.67	4.0
WFM_Ter9_OB5_exp1	2016-06-11T02:20:22	948	1.332	1.263	0.74	0.70	16.0
WFM_Ter9_OB5_exp2	2016-06-11T02:38:13	948	1.259	1.201	0.70	0.71	16.0
WFM_Ter9_OB5_exp3	2016-06-11T02:56:06	948	1.198	1.151	0.71	0.76	16.0

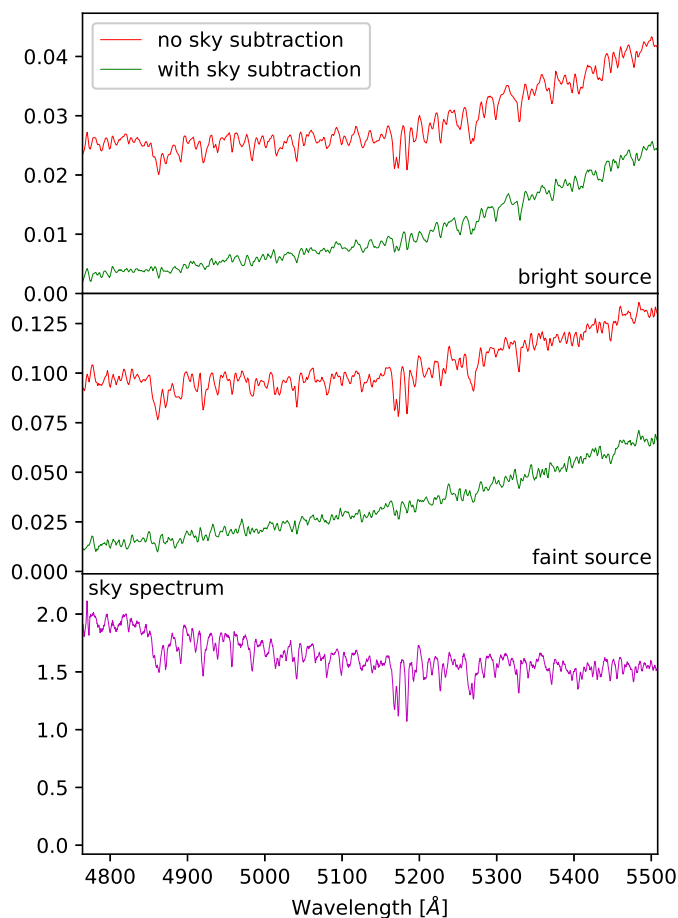


**Fig. 4.** Comparison between sky contribution to bright and faint stellar sources, normalized to their flux at 8604 Å. Scattered stellar light absorption lines can be seen in the sky spectrum, and its subtraction from the actual star spectrum preserves the true line profile.

the critical radius  $cr$  value that optimizes the S/N of the extracted spectra, starting with the default value  $cr = 1.25$ . We noticed that the S/N increases for  $cr < 0.1$  and that the line spread function (LSF) starts to degrade if we adopt  $cr < 0.03$ , therefore we chose  $cr = 0.03$  to optimize the S/N of the extracted spectra without degrading the LSF. We also note that the reconstructed images using  $cr = 0.03$

reveal fainter stars with a stable PSF and higher S/N, delivering a better result than with the default parameters.

In addition, there were three other, simpler resampling methods: nearest, quadratic, and linear. A comparison between these three and the more complex methods discussed above showed that the linear method achieved even better results than ‘renka’ both in terms of the S/N ratio, and the spectral and spatial resolution. Our final resampling was done using the linear method. All of the comparisons were made visually with different source brightness in the regions of the Mg I triplet, H $\alpha$  and Ca II triplet, as well as the spatial resolution and PSF quality, using DS9.

For each of the final cubes, 2D images were created by multiplying the cube by filters transmission curves available in the pipeline: Johnson B, V, Cousins R, I, and a few HST-ACS filters. These images were used to generate color-magnitude diagrams (CMDs) and select Red Giant Branch (RGB) stars to be cross-matched with our previous catalogue.

### 3.3. Extraction of Stellar Spectra

To extract the data from the MUSE datacubes, we employed the PampelMUSE<sup>2</sup> code (Kamann et al. 2013) which is specific to stellar spectra extraction in crowded fields of data cubes such as MUSE. This software aptly deals with the observation of a densely populated stellar field such as a globular cluster. One challenge is the seeing-limited angular resolution of the instrument. A single object is represented by a point spread function (PSF), and the stellar field is a sum of many overlapping PSFs. Even in cases of heavily blended regions, the objects can be recovered using a PSF model if the distance between two neighbor stars is larger than  $0.3 \times \text{FWHM}$ .

This code written in python executes many tasks. In a simplified picture, a datacube is a sum of layers in wavelength of the image. A spaxel contains the entire spectrum, hence contributes to all layers. This method consists in analysing the datacube, layer by layer, performing PSF photometry individually on each layer. In the end all photometric solutions for each layer are combined, building spectra for each of the objects.

In order to get the spectra of sources of interest from the datacube, it is needed to provide an input catalogue with the position and magnitude of these objects, or else a

<sup>2</sup> <https://gitlab.gwdg.de/skamann/pampelmuse>

selection by hand on the image. The coordinates are identified in the list of stars from the NTT 2012 observations (Sect. 2), and the proper motion cleaned CMDs by Rossi et al. (2015). The code locates the stars through a PSF fitting; a degree of confidence is assigned to each object, that can then be resolved in the crowded stellar field, and the spectra to be extracted.

To find a PSF in a crowded field, the program selects a number of relatively isolated objects and fits to them an analytical function. Then an Hermitian of order two is used to smooth the PSF parameters as a function of wavelength.

The last step in the data handling before the analysis is the removal of emission lines and non-stellar features left behind in the previous steps. These lines could introduce noise to the results in the minimum distance method which is the basis of the code ETOILE. The elimination of emission lines was made using a python code, which identifies the lines and cuts them in a region between their two edges, as illustrated in Fig. 5. We proceeded with the elimination of the emission line [O I] 5577.338 Å (Osterbrock et al. 1996) from all sample spectra. A future version of ETOILE may have the option of masking out undesired regions, such as those with their emission lines remaining after the cosmic ray cleaning and sky subtraction.

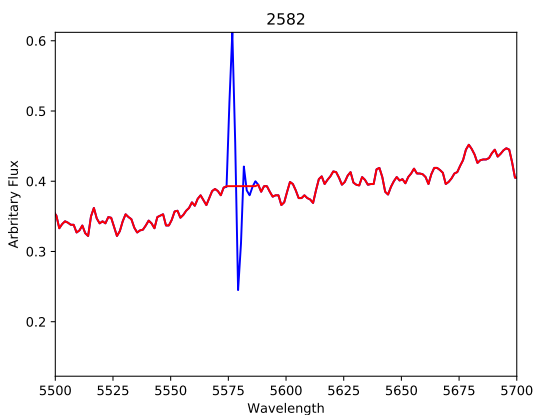


**Fig. 5.** Emission line subtraction from spectrum of star 2582.

Finally, the extracted spectra for each star observed in different nights were combined to get a final 1D spectrum with higher S/N for each star. The combination is done following these steps: Fig. 6 shows the difference in flux levels in the spectra of a same star observed on different nights with the same exposure time but different weather conditions. We accounted for the difference in flux by normalizing them at 5000 Å and adding up all with no airmass-based or S/N-based weight, given that for the same star, there is little variation in S/N. S/N~110 for V~17, and S/N~90 for V~20. All S/N values are given in Table A.1.

#### 4. Analysis

We derived atmospheric parameters via full spectrum fitting with the ETOILE code (Katz et al. 2011). This method is very robust in finding the absolute minimum in a  $\chi^2$  map (e.g. Recio-Blanco et al. 2014; Jofre et al. 2018). The code written in C is a modified version of the HALO (Cayrel et al. 1991) and TGMET (Katz et al. 1998) codes, which

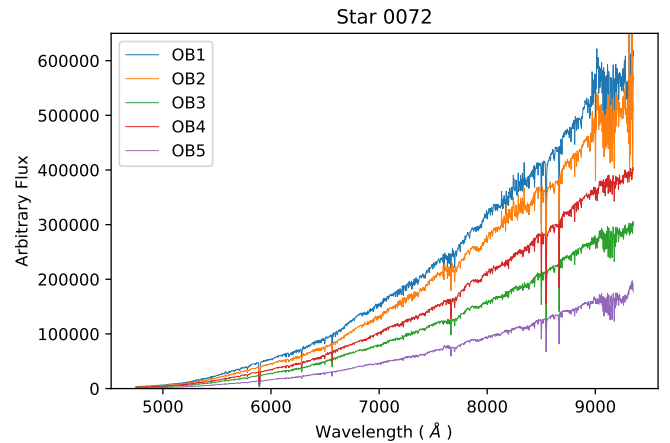


**Fig. 6.** Spectra of Terzan 9 star id 0072 from different data cubes obtained with PampelMUSE.

is obtained by changing the main four procedures: a) the sample star spectrum is compared with the full list of reference spectra, b) the input data are in ascii format, c) the target spectrum does not need to be normalized or calibrated in absolute flux, and d) no input parameters are given. More details on the method for extracting the fundamental stellar parameters ( $T_{\text{eff}}$ ,  $\log g$ ,  $[\text{Fe}/\text{H}]$ ) from the spectra are given in Katz et al. (1998, 2001). In the original code, high resolution spectra of 2000 stars obtained with the ELODIE spectrograph, as presented in Katz et al. (2011), were adopted as reference.

Dias et al. (2015, 2016) implemented two other grids of spectra suitable for the analysis of medium-resolution spectra in the wavelength range 4600-5600 Å: the synthetic spectra by Coelho et al. (2005, hereafter Coelho05) and the MILES grid of observed spectra (Sánchez-Blázquez et al. 2006). We implemented a wavelength-extended version to be run with the Coelho05 library, encompassing the range 3000-18000 Å that covers the region of the MUSE spectra 4800-9300 Å, and it was used in different ways, as explained below.

In summary, the ETOILE code compares the observed spectrum to a list of reference spectra, either observed or synthetic, and finds the most similar ones through a least square of Euclidean distance measure. An example of a fit to a sample spectrum is given in Fig. 7.

##### 4.1. Sample extraction and radial velocities

We were able to extract and combine spectra from the five data cubes for 614 stars. After a selection based on S/N ( $S/N \geq 85$ ) of all final spectra, 90 of them were retained for analysis. The choice of this high S/N was due to better reliability in the parameter derivation. The ETOILE code was run for these spectra in order to derive their stellar parameters. The code first corrects for radial velocity ( $v_r$ ) through cross-correlation with a template spectrum from the library in use. In the present case, we used the MILES library in the wavelength range 4600 - 5600 Å, the synthetic Coelho05 library in the full MUSE range 4860 - 9300 Å, and in the region of the CaII triplet (CaT) 8400 - 8750 Å. The use of these different libraries and wavelength regions has shown that the most reliable method to derive ra-

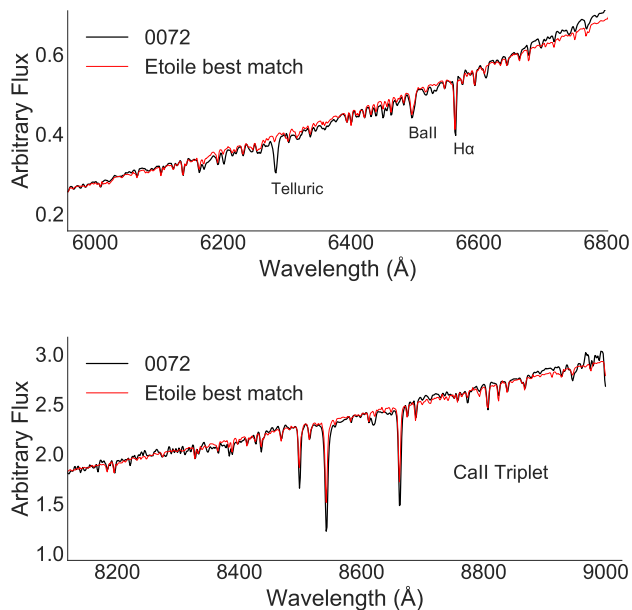


**Fig. 7.** Fit obtained with ETOILE for star 0072 with a good S/N = 129.80. Upper panel: region 6000- 6800 Å where the strongest lines (telluric feature at 6282 Å, BaII 6496.9 Å and H $\alpha$ ) are indicated; lower panel: calcium triplet region.

dial velocities is the comparison of the sample spectra with the synthetic spectra in the CaT region. We concluded this from inspecting a series of spectra from the full initial sample and comparing them individually to reference spectra, verifying the wavelength region with that particular radial velocity value. The results are shown in Fig. 8 as smoothed histograms of radial velocities obtained in the three cases described above.

Fig. 9 shows the radial velocity distribution using the CaT region analysed through the Coelho05 library, for the 90 selected stars. A gaussian fit results in a mean radial velocity value of  $v_r = 49.7 \text{ km s}^{-1}$  and a sigma of  $22 \text{ km s}^{-1}$ . The mean heliocentric radial velocity is  $v_r^h = 58.1 \text{ km s}^{-1}$ . The radial velocity of  $v_r^h = 71.4 \pm 0.4 \text{ km s}^{-1}$  from six stars by Vásquez et al. (2018) is compatible with the present value within uncertainties. A comparison with two stars in common with Vásquez et al. (2018) is reported in Table 3, showing excellent agreement in terms of radial velocities. In conclusion, we suggest that the present value is more accurate given the larger sample of stars taken into account.

For these two stars in common, the metallicities from the present work, derived with ETOILE and from CaT with the same method as Vásquez et al. (2018), that is, by applying their Equation 5 for the metallicity scale by Dias et al. (2016) and their reported values, given in Table 3, show good agreement within uncertainties. The full explanation on how the metallicities are calibrated is given on Sect. 4.4

Finally, the spectra are corrected for the adopted results of radial velocity, which are reported in Table A.2.

**Table 3.** Comparison of radial velocity and metallicity for two stars in common with Vásquez et al. (2018, V+18). The metallicity from V+18 adopts the metallicity scale by Dias et al. (2016).

ID	ID <sub>V+18</sub>	$v_r$ km.s <sup>-1</sup>	$v_r$ (V+18) km.s <sup>-1</sup>	[Fe/H] ETOILE	[Fe/H] CaT	[Fe/H] <sub>V+18</sub>
1322	1_399	75.9 $\pm$ 1.1	74.8 $\pm$ 0.7	-1.52	-1.14	-1.25
1378	1_745	60.8 $\pm$ 1.1	61.9 $\pm$ 0.6	-1.23	-1.34	-1.26

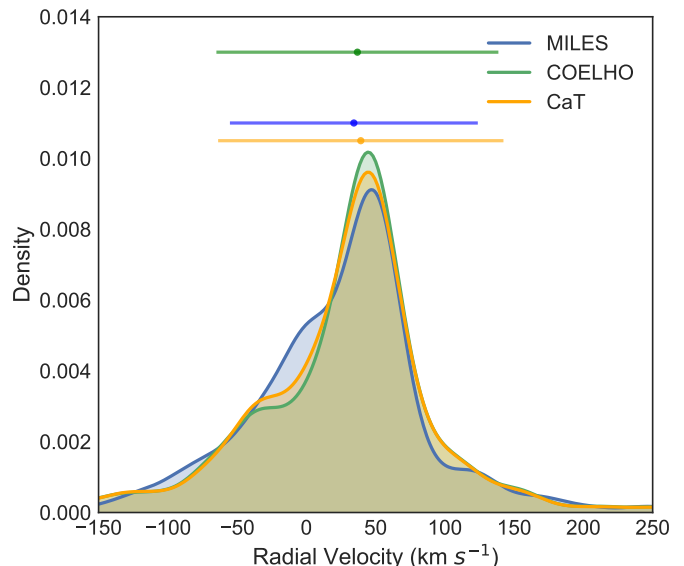


**Fig. 8.** Histograms of radial velocities obtained in the cases: green distribution: MILES library in the range 4860 - 5600 Å; blue distribution: Coelho05 library in the range 4860 - 9000 Å; and yellow distribution: Coelho05 library in the CaT region at 8400 - 8750 Å.

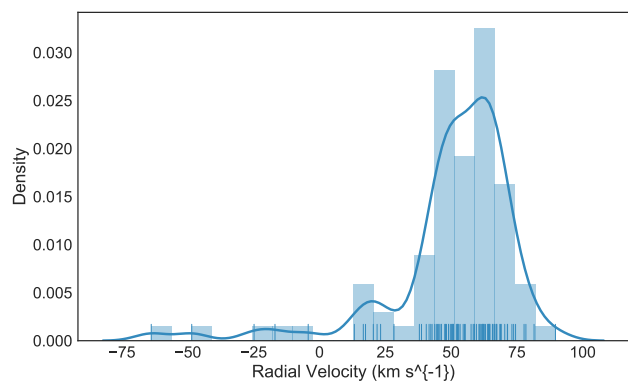


**Fig. 9.** Smoothed histogram of radial velocities obtained with the Coelho05 library in the CaT region at 8400 - 8750 Å. A kernel density estimation (KDE) gaussian fitting the main peak of radial velocity distribution is overlotted.

#### 4.2. Coordinates and proper motions

The X,Y position of stars in the NTT image used to identify the stars in the MUSE data, were transformed to right ascension (RA) and declination (DEC) and matched with the Gaia Data Release 2 (DR2, Gaia collaboration 2018) coor-

dinates, therefore the coordinate values reported in Table A.1 have a high astrometric precision. For the list of 90 selected stars, Gaia data are available.

In the MUSE field, there are 371 stars in the Gaia data that are shown in Fig. 10, where we see a clear cluster, seen as the feature highlighted in blue. Among the 371 Gaia stars, we identified 236 stars with proper motion (PM) information. For this sample, the mean proper motion values derived are:  $\text{pmRA} = -2.212 \pm 0.0851$  mas/yr, and  $\text{pmDE} = -7.425 \pm 0.0851$  mas/yr, in good agreement with derivations by Pérez-Villegas et al. (2019) of  $(-2.314 \pm 0.108, -7.434 \pm 0.068)$  mas/yr and  $(-2.225 \pm 0.038, -7.492 \pm 0.029)$  mas/yr from Vasiliev (2018). Note that the PM value derived uses 236 stars from Gaia which are present in the MUSE field. The values are the same as for the 90 selected member stars, as made evident in the corner plot given in Fig. 15. We note that the previous values by Rossi et al. (2015) of  $(0.0 \pm 0.38, -3.07 \pm 0.49)$  were different from these data, which are more accurate.

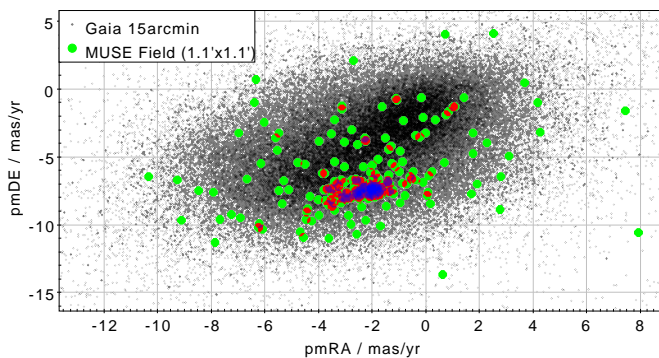


**Fig. 10.** Proper motions from Gaia. Symbols: gray dots: Gaia stars contained within a radius of 15 arcmin from the cluster center; Green dots: Gaia stars in a density representation enclosed in the MUSE field ( $1.1' \times 1.1'$ ). The clustering of stars from Terzan 9 can be seen in red and blue, where blue is the densest part.

In order to identify a final list of member stars, we selected stars from their radial velocity of  $v_r = 58.1 \pm 1.1$  km  $\text{s}^{-1}$ , combined with proper motions of  $\text{pmRA} = -2.21 \pm 0.10$  and  $\text{pmDEC} = -7.42 \pm 0.07$ . We ended up with 67 stars, that are reported in Table A.1.

#### 4.3. Stellar parameters

After radial velocity correction, the stellar spectrum is compared with the spectra of all stars in both libraries: Coelho05 and MILES. The ETOILE code ranks all spectra from the library by similarity ( $S$ ) to the target spectrum.  $S$  is related to  $\chi^2$ , i.e., the most similar spectra have the smallest  $S$  value (for a definition of the similarity parameter, see Katz et al. 1998, and Dias et al. 2015). A weighted mean of the stellar parameters  $T_{\text{eff}}$ ,  $\log g$ ,  $[\text{Fe}/\text{H}]$ , and  $[\alpha/\text{Fe}]$  of the most similar reference spectra is taken as the derived parameter of the target spectrum. The threshold to select the most similar spectra is based on the normalized similarity,  $S/S(1) \leq 1.1$  (Dias et al. 2015), applied to results with both libraries.

The stellar parameters were first derived using the observed library MILES in the wavelength range of 4800-6000

$\text{\AA}$ , containing the MgI triplet lines, which is among the main features commonly used in spectra of galaxies (Mg2, Mgb, Fe5270, Fe5335, Faber et al. 1985). From this procedure we obtained our first set of results.

Using the Coelho05 library, we carried out tests in different spectral regions, as well as with the full spectral range of the MUSE spectra. As a check, we applied these calculations to spectra of the Sun, Arcturus and the metal-rich red giant  $\mu$  Leo (Lecureur et al. 2007). For the synthesis of these spectra, the PFANT code (Barbuy et al. 2018b) was applied. The result indicated that the most reliable region is 6000-6800  $\text{\AA}$ , which is, in fact, the region commonly used to derive stellar parameters from high-resolution spectra (e.g. Barbuy et al. 2018c). This is explained by the following facts: it is widely known that when bluer than 6000  $\text{\AA}$ , the continuum is progressively affected by molecular lines as well as a large number of faint lines. When redder than 6800  $\text{\AA}$ , there are fewer lines, and, particularly fewer lines with well-defined oscillator strengths, and more numerous telluric lines. The stellar parameters were then derived by running ETOILE with the library Coelho05 in the range 6000-6800  $\text{\AA}$ , obtaining a second set of results.

From the final stellar parameters from the two applications (MILES and Coelho05), a mean metallicity obtained from ETOILE along with the two libraries is  $[\text{Fe}/\text{H}] = -1.12 \pm 0.12$ , as shown in Fig. 11. It is important to note that there is a trend for lowering the metallicity as a function of lower S/N in this method. This is the reason for selecting only high S/N > 85 spectra; even so there is still a spread in metallicity values.

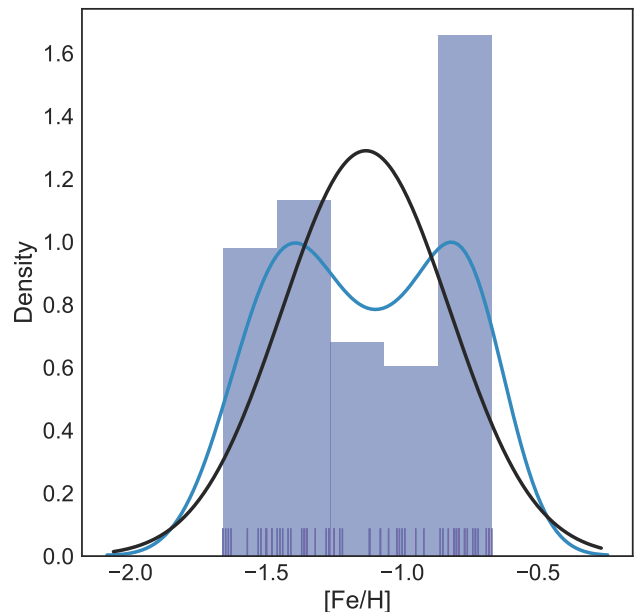


**Fig. 11.** Metallicity distribution of sample stars based on the optical analysis. The black curve represents a gaussian fit centered at a mean value of  $[\text{Fe}/\text{H}] = -1.12 \pm 0.12$ . The blue curve is a KDE gaussian bandwidth estimated using Scott's rule

Finally, in Fig. 14 the metallicity distribution vs. radial velocity distribution is shown, clearly indicating the locus

of the cluster member stars. There is no strong correlation between the possible two peaks in metallicity hinted at in Fig. 11 and radial velocity, meaning that these are not two distinguished groups of similar metallicity and radial velocity values. In Fig. 15, the corner plot of different parameters of the member stars is given.

#### 4.4. Uncertainties

The uncertainties in this paper regarding the stellar parameters are the same as those that have already been described in section 3.2.2 in Dias et al. (2015). The uncertainties on the stellar parameters are computed using the average of squared residuals with the weighted  $1/S^2$  as shown in the equation

$$\sigma_{par(N)} = \sqrt{\frac{1}{M} \frac{\sum_{m=1}^{M_{max}} (par_m - par)^2 \times 1/S_M^2}{\sum_{m=1}^{M_{max}} 1/S_n^2}}, \quad (1)$$

where  $par$  corresponds to the stellar parameters,  $T_{\text{eff}}$ ,  $\log g$ ,  $[\text{Fe}/\text{H}]$ , and  $[\alpha/\text{Fe}]$ , and  $N$  is the number of stars. The  $m$ , and  $M$  are counted as the number of the most similar stars in the library after the criteria of similarity  $S \leq 1.1$  is applied.

#### 4.5. Metallicities from CaT

We normalized the NIR portion of the spectra around the CaT lines in order to perform the techniques described in Vásquez et al. (2015, 2018). The two stronger lines ( $\lambda\lambda$  8542, 8662 Å) were fitted using a combination of a Gaussian and a Lorentzian profile, and the equivalent widths were summed ( $W = W_{8542} + W_{8662}$ ). Since we used the same script as in Vásquez et al. (2018), we were able to directly follow their calibrations, which we briefly describe here. The sum of the equivalent widths was first put into the same scale as Saviane et al. (2012) by applying the relation

$$W_{S12} = 0.97 \times W + 0.21.$$

The  $W_{S12}$  was then corrected by gravity and temperature effects by applying the correction, resulting into the reduced equivalent width

$$W' = W_{S12} + 0.55 \times (V - V_{HB})$$

where  $V_{HB} = 20.35$  mag (Ortolani et al. 1999). The  $W'$  was then converted into metallicity by applying the metallicity scale of Dias et al. (2016) represented by Eq. 5 of Vásquez et al. (2018), that is,

$$[\text{Fe}/\text{H}]_{\text{D16}} = 0.055 \times W'^2 + 0.13 \times W' - 2.68$$

Example of CaT lines are shown in Fig. 12 for star 1378. A typical error in metallicity is of  $\pm 0.1$  dex. The final list of cluster members where the metallicities derived from procedures using the ETOILE code and the CaT measurements are reported in Table A.2, which give a mean value of  $[\text{Fe}/\text{H}] = -1.09 \pm 0.15$ , as shown in Fig. 13.

Finally, a comparison of metallicities for the same stars from the ETOILE code and from CaT lines gives a mean difference of  $[\text{Fe}/\text{H}](\text{ETOILE}) - [\text{Fe}/\text{H}](\text{CaT}) \approx -0.03$  dex.

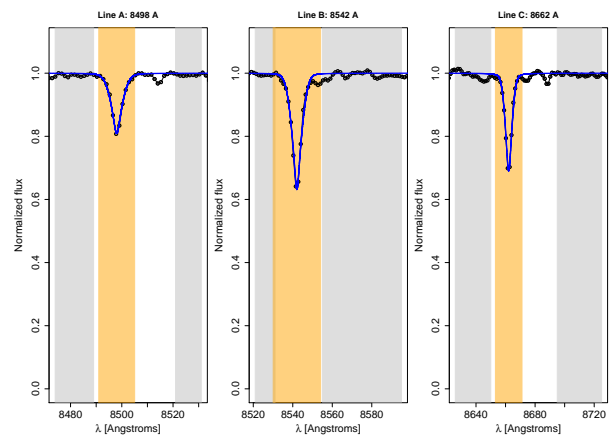


**Fig. 12.** Fit to CaT lines A: 8498 Å; B: 8542 Å, and C: 8662 Å for star 1378 as example. The shaded gray areas show the local continuum regions and the shaded orange areas show the line region defined by Vásquez et al. (2015). The black lines and dots trace the observed spectrum in the rest frame and the blue lines are the best model fit to the data, using a sum of Gaussian and Lorentzian functions. The spectrum has been locally normalized using the highlighted local continuum regions before the fitting. In this analysis we only use the sum of the equivalent widths of the two strongest lines (B+C) following the recipe of Vásquez et al. (2015, 2018).

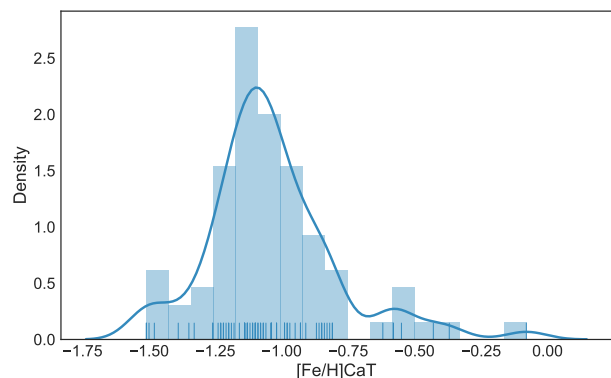


**Fig. 13.** Metallicity distribution of sample stars based on CaT analysis.

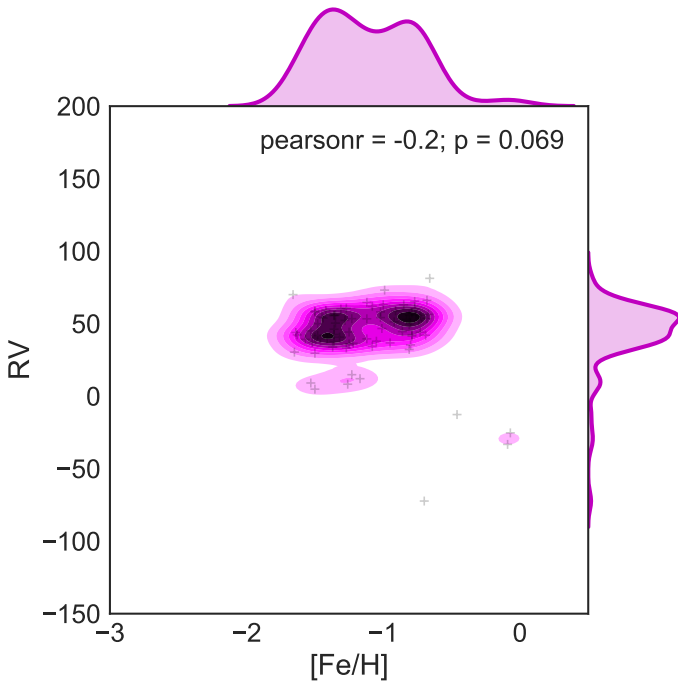
In other words, from ETOILE we get a mean of  $[\text{Fe}/\text{H}] = -1.12 \pm 0.12$  and from CaT we get  $[\text{Fe}/\text{H}] = -1.09 \pm 0.15$ , which are, therefore in excellent agreement.

Fig. 14 shows the metallicity distribution vs. the radial velocity distribution for the identified 67 member stars. Fig. 15 shows a corner plot relating metallicities, proper motions, and radial velocities.

#### 4.6. Color-magnitude diagrams of member stars

In Fig. 16 we compare the I vs. V-I color-magnitude diagram showing all stars where the member stars are highlighted, and the resulting  $\log g$  vs.  $T_{\text{eff}}$  diagram. At the RGB base, a small trend towards high temperatures might be present. The brighter the RGB stars, the closer the





**Fig. 14.** Metallicity distribution based on optical analysis vs. radial velocity distribution, for identified member stars.

isochrones get to the more metal-rich ones, again indicating that the metallicity is not bimodal and that the spread is due to S/N effects. On the right panel, member stars identified in the Gaia survey, are plotted with Gaia colors  $G$  vs.  $BR-RP$ . Dartmouth isochrones of 13 Gyr,  $[Fe/H]=-2.0$  and  $[Fe/H]=-1.0$  are overplotted. The  $I$  values were corrected by  $A_I$  cf. Schlafly & Finkbeiner (2011)<sup>3</sup>; for the Gaia magnitudes no corrections were applied. In this Fig. we clearly see the RGB stars. A BHB appears more clearly present in Fig. 16b, confirming earlier evidence by Ortolani et al. (1999).

## 5. Discussion

Photometric data indicate a broad range of metallicities: from  $V$  vs.  $V-I$  CMDs, Ortolani et al. (1999) deduced a metallicity of  $[Fe/H]\sim-2.0$ , Valenti et al. (2007) instead derived  $[Fe/H]\sim-1.2$  from  $K_s$  vs.  $J-K_s$  CMDs; Bica et al. (1998) derived  $[Z/Z_\odot]=-1.01$  using integrated spectra of CaT lines. High-resolution spectroscopic analyses based on CaT lines from the literature are available: Armandroff & Zinn (1998) obtained  $[Fe/H]=-0.99$ , and from 6 stars, Vásquez et al. (2018) report  $Fe/H]=-1.08\pm 0.14$ ,  $-1.21\pm 0.15$ ,  $-1.16\pm 0.21$ , on the scales of Dias et al. (2016), Saviane et al. (2012), and their own. The compilation by Harris (1996, 2010 edition) reports  $[Fe/H]=-1.05$ , whereas average metallicity compiled by Carretta et al. (2009), adopting a value from Harris (1996) from before 2010, was given as  $[Fe/H]=-2.07\pm 0.09$ . In the present work, the metallicity derived from the 67 selected member stars turned out to be of  $[Fe/H]=-1.12\pm 0.12$  from the optical and  $[Fe/H]=-1.09\pm 0.15$  from CaT lines, therefore, a final metallicity of  $[Fe/H]=-1.10\pm 0.15$  was adopted.

<sup>3</sup>

<https://irsa.ipac.caltech.edu/applications/DUST>

The radial velocity of our sample stars was double-checked with synthetic spectra exhaustively, therefore, we suggest that our value of  $v_r^h = 58.1\pm 1.1$  km s<sup>-1</sup> is more robust than the higher value of  $v_r = 71.4$  km s<sup>-1</sup>, given in Vásquez et al. (2018), due to the higher numbers of stars.

Terzan 9 is now included in the list of moderately metal-poor globular clusters with a BHB similar to HP 1 (Barbuy et al. 2016), NGC 6522 (Barbuy et al. 2014), and NGC 6558 (Barbuy et al. 2018c). Therefore, Terzan 4 continues, so far, to be the most metal-poor cluster in the Galactic bulge, with  $[Fe/H]=-1.6$  (Origlia & Rich 2004). Other potential bulge clusters with metallicities below that of Terzan 4, and within 3.5 kpc from the Galactic center, specifically NGC 6144, NGC 6273, NGC 6287, NGC 6293, NGC 6293, NGC 6333, NGC 6541, are classified as halo intruders in Bica et al. (2016). The orbital classification by Pérez-Villegas et al. (2019) determines these clusters as inner/outer halo, thick disk or disk, and none of them are classified as a bulge member. As for NGC 6681, it has a radial velocity of 216.62 km/s, and apogalactic distance of 4.97 kpc (Baumgardt et al. 2019), which might indicate that it is a halo intruder.

Terzan 9 has a blue HB, but not an extended one (see Ortolani et al. 1999). The moderately metal-poor metallicity found for Terzan 9 correspond essentially to the lower end of the metallicity distribution of the bulk bulge stellar population. As a matter of fact, due to a fast chemical enrichment in the Galactic bulge, such as the one modeled by e.g. Cescutti et al. (2008), the iron abundance of  $[Fe/H]\sim-1.3$  is reached very fast, and stellar populations start to form in more significant numbers from there on, as confirmed by metallicity distribution functions (MDF) given in Zoccali et al. (2008, 2017), Hill et al. (2011), Ness et al. (2013), Rojas-Arriagada et al. (2014, 2017) - see also Barbuy et al. (2018a).

The derivation of Mg-to-iron is based on the fitting of the MgI triplet lines (see Dias et al. 2015, 2016). In Fig. 17, the distribution of enhancement in the  $\alpha$ -element Mg is shown with a mean value of  $[Mg/Fe]=+0.27\pm 0.03$ . The sigma of the distribution results is also  $\pm 0.03$ . This enhancement is similar to those reported in the Galactic bulge by Barbuy et al. (2018a) and Schultheis et al. (2017). This indicates that the stars in Terzan 9 were formed from gas resulting from an early fast chemical enrichment by core-collapse supernovae.

## 6. Conclusions

We obtained MUSE datacubes for the bulge compact globular cluster Terzan 9. Using the software pampelMUSE by Kamann et al. (2013, 2018), we were able to extract the spectra of over 600 stars. The sample was reduced to 67 member stars by selecting spectra with  $S/N>85$  and with compatible radial velocities and proper motions. These spectra were analysed based on a full spectrum fitting with the ETOILE code in the area of 4600-5600 Å, compared with a grid of observed spectra (MILES, Sánchez-Blázquez et al. 2006). In the area of 6000-6800 Å, they were compared with a grid of synthetic spectra by Coelho et al. (2005, Coelho05). The CaT lines were also measured in order to obtain an independent derivation of metallicity. Both methods give very close mean results, with an adopted mean of  $[Fe/H]=-1.10\pm 0.15$ . This mean value is the outcome of the combination of a range of values where, in particular with regard to the optical region, two metallicity peaks are

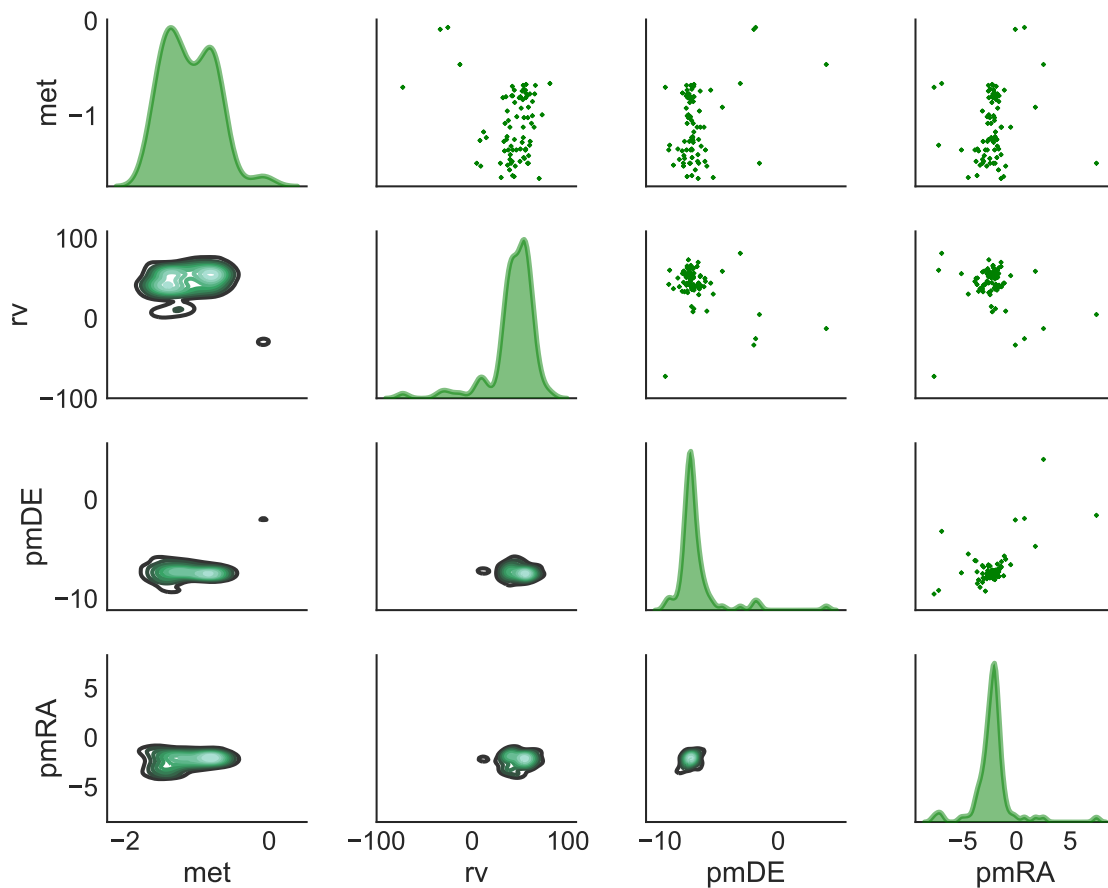


**Fig. 15.** Corner plot: metallicity, proper motion and radial velocities.

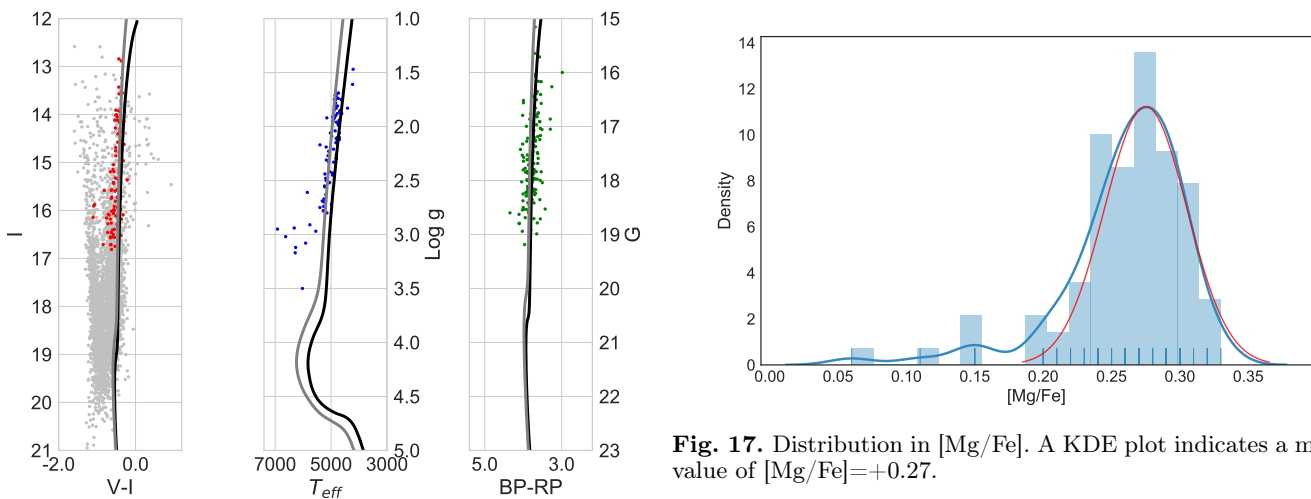


**Fig. 16.** I vs. V-I color-magnitude diagram showing all stars (gray) and member stars (red) (left panel), compared with the  $\log g$  vs.  $T_{\text{eff}}$  diagram (middle panel), and CMD in Gaia magnitudes and colors G vs. BP-RP for the stars in common (right panel). Dartmouth isochrones of 13 Gyr, and  $[\text{Fe}/\text{H}]=-1.0$  are overplotted in black and isochrones of 13 Gyr, and  $[\text{Fe}/\text{H}]=-2.0$  are overplotted in gray.

**Fig. 17.** Distribution in  $[\text{Mg}/\text{Fe}]$ . A KDE plot indicates a mean value of  $[\text{Mg}/\text{Fe}]=+0.27$ .

seen. In order to confirm metallicities, further observations with high resolution spectroscopy are of great interest. The present paper allows for a reliable target selection for such studies.

We were able to derive a mean heliocentric radial velocity of  $v_r^h = 58.1 \pm 1.1 \text{ km s}^{-1}$ , which is somewhat lower than the value from Vásquez et al. (2018) based on 6 stars, but the values are in agreement within uncertainties. These metallicities place Terzan 9 as a new member of the mod-

erately metal-poor clusters with a blue horizontal branch that are found in the Galactic bulge.

*Acknowledgements.* We are grateful to David Katz for helpful comments on the Etoile code, and to Angeles Pérez-Villegas for help with the proper motion and orbital information. HE, BB, EB and EC acknowledge partial financial support, grants and fellowships from FAPESP, CNPq and CAPES - Finance code 001. HE and EC are grateful for their visit to ESO in Santiago, within ESO's office for science programme, under supervision of B. Dias.

## References

- Armandroff, T.E., Zinn, R. 1988, *AJ*, 96, 92  
 1999, *A&AS*, 140, 261  
 Barbuy, B., Chiappini, C., Cantelli, E., et al. 2014, *A&A*, 570, A76  
 Barbuy, B., Cantelli, E., Vemado, A., et al. 2016, *A&A*, 591, A53  
 Barbuy, B., Chiappini, C., Gerhard, O. 2018a, *ARA&A*, 56, 223  
 Barbuy, B., Trevisan, J., de Almeida, A. 2018b, *PASA*, 35, 46  
 Barbuy, B., Muniz, L., Ortolani, S. et al. 2018c, *A&A*, 619, A178  
 Bica, E., Bonatto, C., Barbuy, B., Ortolani, S. 2006, *A&A*, 450, 105  
 Baumgardt, H., Hilker, M., Sollima, A., Bellini, A. 2019, *MNRAS*, 482, 5138  
 Buck, T., Ness, M., Macciò, A.V., Obreja, A., Dutton, A.A. 2018, *ApJ*, 861, 88  
 Cayrel, R., Perrin, M.-N., Barbuy, B., Buser, R. 1991, *A&A*, 247, 108A&A  
 Carretta, E., Bragaglia, A., Gratton, R., D'Orazi, V., Lucatello, S. 2009, *A&A*, 508, 695  
 Cescutti, G., Matteucci, F., Lanfranchi, G.A., McWilliam, A. 2008, *A&A* 491:401  
 Coelho, P., Barbuy, B., Meléndez, J., Schiavon, R.P., Castilho, B.V. 2005, *A&A*, 443, 735  
 Dias, B., Barbuy, B., Saviane, I., et al. 2015, *A&A*, 573, A13  
 Dias, B., Barbuy, B., Saviane, I., et al. 2016, *A&A*, 590, A9  
 Faber, S.M., Friel, E., Burstein, D., Gaskell, C.M. 1985, *ApJ*, 57, 711  
 Gaia Collaboration, Brown, A. G. A., Vallenari, A., et al. 2018a, *A&A*, 616, A1  
 Harris W. 1996, *AJ*, 112, 1487 (edition of 2010)  
 Hill V, Lecureur A, Gómez A, et al. 2011. *A&A* 534:A80  
 Jofre, O., Heiter, U., Soubiran, C. 2018, arXiv:1811.08041  
 Kamann, S., Wisotzki, L., Roth, M. M., 2013, *A&A* 549, A71  
 Kamann, S., Husser, T.-O., Dreizler, S. et al. 2018, *MNRAS*, 473, 5591  
 Katz, D., Soubiran, C., Cayrel, R., Adda, M., Cautain, R., 1998, *A&A* 338, 151  
 Katz, D. 2001, *JAD*, 7, 8  
 Katz, D., Soubiran, C., Cayrel, R., Barbuy, B., Friel, E., Bienaymé, O., Perrin, M. N., 2011, *A&A* 525, A90  
 Kerber, L.O., Nardiello, D., Ortolani, S., et al. 2018, *ApJ*, 853, 15  
 Kerber, L.O., Libralato, M., Ortolani, S., et al. 2019, *MNRAS*, 484, 5530  
 Kunder, A., Valenti, E., Dall'Ora, M. et al. 2018, *SSRv*, 214, 90  
 Lecureur, A., Hill, V., Zoccali, M. et al. 2007, *A&A*, 465, 799  
 Ness M, Freeman K, Athanassoula E, et al. 2013a. *MNRAS* 430:836–857  
 Origlia, L., Rich, R.M. 2004, *AJ*, 127, 3422  
 Ortolani, S., Bica, E., Barbuy, B., 1999, *A&AS*, 138, 267  
 Osterbrock, D.E., Fulbright, J.P., Martel, A.R. et al. 1996, *PASP*, 108, 277  
 Pérez-Villegas, A., Rossi, L., Ortolani, S. et al. 2018, *PASA*, 35, 21  
 Pérez-Villegas, A., Barbuy, B., Kerber, L. et al. 2019, *MNRAS*, accepted  
 Recio-Blanco, A. 2014, *IAU Symp.* 298, 366  
 Renzi, A., Gennaro, M., Zoccali, M. et al. 2018, *ApJ*, 863, 16  
 Rojas-Arriagada A, Recio-Blanco A, Hill V, et al. 2014. *A&A* 569:A103–119  
 Rojas-Arriagada A, Recio-Blanco A, et al. 2017. *A&A* 601:A140  
 Rossi, L., Ortolani, S., Bica, E., Barbuy, B., Bonfanti, A. 2015. *MNRAS*, 450, 3270  
 Sánchez-Blázquez, P., Peletier, R.F., Jiménez-Vicente, J., et al., 2006, *MNRAS*, 371, 703  
 Saviane, I., da Costa, G.S., Held, E.V. et al. 2012, *A&A*, 540, A27  
 Schlafly, E., Finkbeiner, D.P. 2011, *ApJ*, 737, 103  
 Schultheis, M., Rojas-Arriagada, A., García-Pérez, A., et al. 2017, *A&A*, 600, A14  
 Valenti, E., Ferraro, F.R., Origlia, L. 2007, *AJ*, 133, 1287  
 Vásquez, S., Zoccali, M., Hill, V. et al. 2015, *A&A*, 580, A121  
 Vásquez, S., Saviane, I., Held, E.V. et al. 2018, *A&A*, 619, A13  
 Vasiliev, E. 2018, *MNRAS*, 484, 2832  
 Zoccali, M., Hill, V., Lecureur, A. et al. 2008, *A&A*, 486, 177  
 Zoccali, M., Vásquez, S., Gonzalez, O.A. et al. 2017, *A&A*, 599, A12

## Appendix A: Extracted stars from the MUSE datacubes

**Table A.1.** Identified member stars from MUSE datacubes selected with S/N>85. Columns correspond to: ID from NTT 2012 data, coordinates (RA,DEC-J2000), proper motions from Gaia, NTT pixels x, y, NTT V, NTT V-I, and S/N.

ID	RA (J2000)	DEC (J2000)	pmRA	pmDEC	X	Y	V	V-I	S/N
0072	270.41522393678054	-26.83960326833801	-1.6470	-7.1760	1114.09	991.63	17.87	3.812	129.80
0081	270.40828978697527	-26.83592435071913	-1.8160	-7.1100	929.55	1101.25	18.42	3.841	125.00
0084	270.41578613193025	-26.83405140131479	-2.5750	-7.6500	1129.81	1157.05	18.74	3.937	114.13
0089	270.39921802548110	-26.83204463546964	-2.1770	-7.3860	687.86	1217.57	18.58	3.717	114.03
0092	270.40840223869230	-26.83177706400694	-2.0010	-7.4560	932.48	1225.10	18.88	4.252	121.02
0437	270.40307930558885	-26.84742893173680	-1.8330	-7.4950	790.31	757.66	17.94	3.820	106.96
0473	270.41432441417822	-26.84421846865514	-3.0010	-7.9650	1090.16	853.74	19.68	3.417	99.41
0513	270.40034269441361	-26.84074036414967	-2.2920	-7.4720	717.94	957.50	18.12	3.950	117.32
0520	270.41170073374064	-26.84023870564067	-2.4930	-7.5020	1020.38	972.22	17.97	3.688	129.40
0549	270.41867198860143	-26.83655980866259	-2.0500	-7.5950	1206.10	1082.43	18.34	3.984	122.03
0554	270.39678117444549	-26.83615846721820	-2.1590	-7.5650	622.57	1094.94	18.25	3.849	113.81
0571	270.41484913724622	-26.83505477091640	-1.7740	-7.5350	1104.23	1127.62	17.69	4.144	116.83
0578	270.41814729715378	-26.83448619589934	-2.6740	-7.1830	1192.40	1144.92	18.47	4.122	124.17
0582	270.40105497443244	-26.83408484711128	-2.0170	-8.0870	736.12	1156.14	17.82	3.900	104.30
0584	270.41260029354157	-26.83395106386613	-1.4360	-6.8510	1044.23	1160.69	19.74	4.040	122.81
0595	270.41147584179771	-26.83294768449528	-3.1640	-8.3520	1014.50	1190.66	20.21	3.861	101.16
0610	270.40585328417666	-26.83164327803886	-2.6140	-7.7440	864.91	1229.44	18.27	3.985	116.47
0611	270.40315427957711	-26.83147604535684	-2.6990	-7.5050	792.25	1234.08	19.50	3.688	108.72
0615	270.41642328041041	-26.83107468591398	-2.2590	-7.1160	1146.62	1246.95	18.63	4.089	120.39
0631	270.42020856001682	-26.82940233961694	-1.4360	-6.7630	1247.46	1296.56	18.68	3.530	88.71
0645	270.41293762517887	-26.82746238703481	-2.4270	-7.2970	1053.09	1354.89	19.53	3.807	85.38
0936	270.40296684444041	-26.83475376096855	-2.1910	-7.6940	787.64	1136.18	17.35	4.109	108.45
1342	270.41282518149904	-26.84361649668046	-3.1550	-7.4820	1050.16	871.39	19.54	3.358	112.85
1353	270.40570334248764	-26.84298107834307	-2.0320	-7.2650	860.67	890.05	19.27	3.669	125.42
1368	270.40915191171359	-26.84181056153792	-2.0550	-7.3130	952.73	925.10	17.73	3.714	140.45
1380	270.40821481905323	-26.84090758315861	-2.3690	-7.6940	927.83	952.88	18.55	3.358	122.89
1399	270.40349166142846	-26.83963671249548	-2.4830	-7.9150	801.46	990.74	19.76	3.821	109.47
1406	270.41121346685679	-26.83936915895905	-2.6190	-6.5930	1007.24	998.86	17.34	3.912	100.73
1413	270.40401647407731	-26.83886749437426	-1.6550	-7.3100	815.57	1013.86	20.19	3.636	97.36
1414	270.41739773041394	-26.83880060559504	-1.8270	-7.2750	1172.89	1015.09	19.36	3.793	127.92
1426	270.40802739886061	-26.83793104786989	-1.6750	-7.0070	922.82	1041.32	19.62	3.630	110.36
1433	270.41754764447046	-26.83752971128347	-3.0530	-6.8120	1176.21	1053.57	19.48	3.204	112.48
1441	270.41147584179771	-26.83692770373768	-1.8900	-7.1330	1014.86	1071.40	17.49	3.923	117.52
1447	270.42043342100408	-26.83645947343477	-2.1240	-7.1800	1253.94	1085.56	19.00	3.681	95.24
1448	270.41151332384356	-26.83572367904923	-4.4920	-5.4910	1015.41	1107.86	20.09	3.801	101.22
1514	270.40776500966109	-26.83184395693179	-1.6220	-7.7590	915.49	1223.40	19.15	4.193	120.53
1545	270.40735268158420	-26.83003783411370	-2.7280	-7.4070	904.67	1277.56	19.82	4.459	97.37
2009	270.40877707631000	-26.84067347647692	-3.6420	-8.4780	942.11	959.88	20.09	3.377	85.56
2011	270.41027640464006	-26.84037248146045	-2.5990	-6.7240	982.66	968.88	18.39	3.704	134.41
2013	270.40559088598837	-26.84033903752032	-0.5410	-6.5740	857.80	969.23	18.46	3.706	131.43
2032	270.41080116118627	-26.83816516022189	-2.3340	-7.1630	996.01	1034.08	17.77	3.760	129.99
2034	270.41559873410057	-26.83803138179427	-1.8210	-7.2890	1124.13	1038.38	18.78	3.591	130.93
2038	270.40971416066765	-26.83689425878022	-2.7190	-7.7350	967.22	1072.12	19.62	3.568	110.74
2055	270.40086753309708	-26.83562334308101	-1.8830	-7.3890	731.65	1110.99	18.01	3.885	117.00
2062	270.40836475480876	-26.83448619589934	-3.1760	-6.6610	931.93	1144.49	20.25	4.076	97.77
2352	270.41053878345559	-26.84568894221631	-3.3940	-8.8530	989.78	809.38	19.38	3.284	109.77
2355	270.41379968677040	-26.84502109297108	-2.1480	-8.0110	1076.29	829.32	19.03	3.459	136.97
2518	270.41589857036234	-26.84053970101285	-1.4380	-6.7830	1132.82	963.10	20.05	3.554	89.15
2523	270.40405396052904	-26.84010492966281	-2.7670	-7.9990	816.13	976.28	19.84	3.724	113.03
2525	270.40802739886061	-26.83993770946819	-3.5260	-8.1130	922.68	981.08	18.97	3.557	130.86
2561	270.41196310666669	-26.83468686976047	-3.7640	-6.1900	1027.36	1138.66	20.40	3.656	90.63
2562	270.40157980722722	-26.83461997851290	-1.9920	-7.2260	750.53	1140.22	19.18	3.456	106.00
2573	270.41233792325039	-26.83318180714274	-1.7830	-6.5100	1037.44	1183.96	20.57	4.048	86.81
2575	270.40971416066765	-26.83234565261057	-3.1110	-7.9170	967.65	1208.54	19.98	4.012	109.40
2748	270.41245036779372	-26.83956982417065	-3.8680	-6.1480	1040.01	992.71	18.99	3.412	121.33
2848	270.40881455994997	-26.83679392384860	-1.3960	-6.2670	943.93	1075.06	20.03	3.633	92.35
2851	270.40990157587862	-26.83318180714274	-2.1280	-7.6950	972.15	1183.44	18.23	4.281	112.67
2903	270.41121346685679	-26.84221188294944	-3.6720	-7.2970	1007.51	913.48	19.93	3.361	92.13
2963	270.41147584179771	-26.83498787988597	-2.0390	-7.2200	1014.40	1129.59	19.16	3.956	133.76
2968	270.40202966045496	-26.83181051047429	-2.1270	-7.6880	762.65	1224.70	19.53	3.612	108.05
3042	270.40862714152860	-26.84211155272999	-2.4570	-6.7110	938.05	916.28	20.07	3.516	94.47
3068	270.40937681189303	-26.83361660506254	-1.1350	-5.7000	958.32	1170.29	18.39	4.245	129.01
3088	270.41462425646279	-26.83752971128347	-1.9910	-7.4270	1098.60	1053.20	19.63	3.565	115.52
3104	270.41346235971645	-26.83773037975444	-1.1950	-7.6990	1067.02	1047.56	19.44	3.429	104.55
3162	270.40746513496180	-26.84254631637180	-2.5720	-7.5880	907.93	903.03	16.76	3.917	99.54
3187	270.41020143906485	-26.83769693503397	-1.9390	-7.7700	980.88	1048.00	17.63	3.717	110.81
3194	270.41275021893512	-26.84047281322153	-1.7490	-7.7720	1048.33	965.88	16.95	4.072	102.53

**Table A.2.** Identified members stars from MUSE datacubes selected with  $S/N > 85$ . Columns correspond to: ID and results from the present work:  $v_r^h$  (km s $^{-1}$ ),  $T_{\text{eff}}$  (K),  $\log g$ , [Fe/H], [Mg/Fe], and [Fe/H] $_{\text{CaT}}$ .

ID	$v_r$ (km s $^{-1}$ )	$T_{\text{eff}}$ (K)	$\log g$	[Fe/H]	[Mg/Fe]	EWa	EWb	EW'	[Fe/H] $_{\text{CaT}}$
0072	63.06	4660 ± 42	1.99 ± 0.15	-0.85 ± 0.07	0.27 ± 0.03	3.095 ± 0.114	2.365 ± 0.102	5.460 ± 0.153	-1.20 ± 0.09
0081	35.38	4893 ± 49	2.21 ± 0.13	-0.80 ± 0.06	0.24 ± 0.02	2.994 ± 0.161	2.385 ± 0.141	5.377 ± 0.214	-1.07 ± 0.12
0084	32.17	4885 ± 52	2.33 ± 0.13	-0.81 ± 0.07	0.24 ± 0.02	2.963 ± 0.138	2.240 ± 0.121	5.203 ± 0.183	-1.06 ± 0.11
0089	66.10	4988 ± 28	2.72 ± 0.10	-0.68 ± 0.05	0.21 ± 0.02	3.626 ± 0.138	3.135 ± 0.161	6.761 ± 0.212	-0.08 ± 0.16
0092	49.20	4788 ± 46	2.15 ± 0.12	-0.81 ± 0.07	0.26 ± 0.02	3.128 ± 0.143	2.410 ± 0.126	5.539 ± 0.190	-0.81 ± 0.12
0437	57.47	4628 ± 36	2.12 ± 0.12	-0.79 ± 0.06	0.27 ± 0.03	3.198 ± 0.112	2.411 ± 0.096	5.610 ± 0.148	-1.09 ± 0.09
0473	59.01	5220 ± 90	2.19 ± 0.17	-1.42 ± 0.10	0.30 ± 0.03	2.489 ± 0.143	2.040 ± 0.118	4.529 ± 0.185	-1.14 ± 0.10
0513	44.50	4630 ± 37	2.06 ± 0.12	-0.86 ± 0.06	0.29 ± 0.03	3.144 ± 0.139	2.293 ± 0.117	5.437 ± 0.182	-1.13 ± 0.10
0520	58.13	4670 ± 66	1.69 ± 0.20	-1.02 ± 0.10	0.29 ± 0.03	3.121 ± 0.140	2.389 ± 0.125	5.510 ± 0.188	-1.14 ± 0.11
0549	54.18	4728 ± 49	1.88 ± 0.18	-1.02 ± 0.08	0.30 ± 0.03	3.081 ± 0.118	2.390 ± 0.106	5.471 ± 0.159	-1.04 ± 0.10
0554	56.09	4934 ± 39	2.45 ± 0.12	-0.81 ± 0.06	0.24 ± 0.02	3.154 ± 0.132	2.647 ± 0.119	5.801 ± 0.178	-0.87 ± 0.11
0571	60.37	4524 ± 49	1.88 ± 0.17	-0.77 ± 0.08	0.29 ± 0.03	3.213 ± 0.132	2.499 ± 0.121	5.712 ± 0.179	-1.11 ± 0.10
0578	61.99	4554 ± 62	1.75 ± 0.21	-1.08 ± 0.09	0.30 ± 0.03	3.071 ± 0.150	2.361 ± 0.143	5.432 ± 0.207	-1.02 ± 0.12
0582	56.05	4652 ± 44	1.94 ± 0.14	-0.76 ± 0.07	0.24 ± 0.03	3.325 ± 0.103	2.633 ± 0.087	5.958 ± 0.135	-1.08 ± 0.09
0584	64.72	4972 ± 87	2.09 ± 0.22	-1.12 ± 0.10	0.38 ± 0.03	3.222 ± 0.147	2.509 ± 0.138	5.761 ± 0.231	-1.04 ± 0.12
0595	39.55	5286 ± 39	2.74 ± 0.12	-1.46 ± 0.06	0.28 ± 0.01	2.797 ± 0.155	2.199 ± 0.136	4.996 ± 0.206	-0.84 ± 0.13
0610	53.41	4767 ± 36	2.26 ± 0.12	-0.68 ± 0.06	0.24 ± 0.02	3.185 ± 0.144	2.404 ± 0.127	5.589 ± 0.192	-0.99 ± 0.11
0611	60.67	5134 ± 78	2.27 ± 0.16	-1.27 ± 0.08	0.27 ± 0.03	2.698 ± 0.124	2.021 ± 0.097	4.719 ± 0.158	-1.09 ± 0.10
0615	56.39	5056 ± 46	2.42 ± 0.12	-0.67 ± 0.06	0.24 ± 0.02	2.080 ± 0.106	2.377 ± 0.094	5.471 ± 0.141	-0.95 ± 0.09
0631	70.03	5348 ± 43	2.78 ± 0.13	-1.66 ± 0.06	0.29 ± 0.01	2.523 ± 0.098	2.209 ± 0.230	4.732 ± 0.250	-1.35 ± 0.12
0645	54.05	5684 ± 42	2.97 ± 0.09	-0.72 ± 0.05	0.15 ± 0.02	2.890 ± 0.127	2.281 ± 0.125	5.171 ± 0.178	-0.81 ± 0.11
0936	65.37	4264 ± 33	1.83 ± 0.14	-0.77 ± 0.07	0.24 ± 0.03	3.325 ± 0.103	2.633 ± 0.087	5.958 ± 0.135	-1.08 ± 0.09
1342	57.98	4821 ± 64	1.71 ± 0.19	-1.50 ± 0.10	0.30 ± 0.04	2.483 ± 0.117	1.919 ± 0.099	4.403 ± 0.153	-1.26 ± 0.09
1353	37.79	4714 ± 134	1.81 ± 0.34	-1.36 ± 0.15	0.26 ± 0.05	2.740 ± 0.160	2.098 ± 0.161	4.837 ± 0.227	-1.10 ± 0.12
1368	37.91	4589 ± 70	1.85 ± 0.21	-1.05 ± 0.10	0.28 ± 0.04	2.859 ± 0.146	2.154 ± 0.117	5.013 ± 0.188	-1.48 ± 0.09
1380	34.38	5498 ± 410	2.17 ± 0.38	-1.08 ± 0.25	0.20 ± 0.07	2.628 ± 0.152	2.368 ± 0.161	4.996 ± 0.222	-1.24 ± 0.12
1399	54.69	4796 ± 104	1.90 ± 0.27	-1.45 ± 0.12	0.29 ± 0.03	2.688 ± 0.134	2.092 ± 0.119	4.781 ± 0.179	-0.97 ± 0.11
1406	52.26	4582 ± 62	1.87 ± 0.17	-0.74 ± 0.07	0.32 ± 0.04	3.298 ± 0.123	2.660 ± 0.127	5.958 ± 0.176	-1.08 ± 0.10
1413	56.02	5110 ± 78	2.33 ± 0.18	-1.35 ± 0.09	0.27 ± 0.03	2.430 ± 0.165	1.879 ± 0.161	4.309 ± 0.231	-1.10 ± 0.13
1414	53.88	4788 ± 96	1.72 ± 0.27	-1.44 ± 0.14	0.27 ± 0.04	2.774 ± 0.129	2.200 ± 0.116	4.974 ± 0.173	-0.99 ± 0.11
1426	39.18	4753 ± 76	1.70 ± 0.22	-1.57 ± 0.12	0.29 ± 0.04	2.650 ± 0.193	2.095 ± 0.213	4.745 ± 0.287	-1.04 ± 0.16
1433	41.82	6586 ± 96	3.12 ± 0.11	-1.48 ± 0.08	0.24 ± 0.03	—	—	—	—
1441	42.03	4622 ± 44	1.86 ± 0.12	-0.69 ± 0.07	0.33 ± 0.03	3.430 ± 0.162	2.703 ± 0.136	6.134 ± 0.212	-0.93 ± 0.13
1447	52.27	5217 ± 49	2.50 ± 0.12	-1.28 ± 0.06	0.27 ± 0.02	2.828 ± 0.129	2.288 ± 0.162	5.116 ± 0.207	-1.02 ± 0.12
1448	30.36	4865 ± 76	1.85 ± 0.24	-1.65 ± 0.15	0.29 ± 0.05	—	—	—	—
1514	41.44	5244 ± 106	2.48 ± 0.18	-0.79 ± 0.10	0.20 ± 0.04	3.005 ± 0.183	2.317 ± 0.180	5.322 ± 0.256	-0.85 ± 0.15
1545	46.67	5072 ± 42	2.52 ± 0.12	-1.01 ± 0.07	0.25 ± 0.02	3.139 ± 0.115	2.511 ± 0.111	5.650 ± 0.180	-0.37 ± 0.12
2009	50.38	5277 ± 54	2.44 ± 0.14	-1.35 ± 0.07	0.28 ± 0.02	2.466 ± 0.142	1.906 ± 0.149	4.371 ± 0.206	-1.10 ± 0.12
2011	44.21	4776 ± 78	1.73 ± 0.22	-1.25 ± 0.15	0.29 ± 0.04	2.972 ± 0.135	2.457 ± 0.122	5.429 ± 0.182	-1.04 ± 0.11
2013	53.35	4859 ± 96	1.75 ± 0.25	-1.12 ± 0.15	0.28 ± 0.04	2.861 ± 0.147	2.269 ± 0.148	5.130 ± 0.209	-1.20 ± 0.11
2032	50.53	4774 ± 45	2.11 ± 0.12	-0.80 ± 0.07	0.26 ± 0.02	3.166 ± 0.147	2.525 ± 0.135	5.692 ± 0.199	-1.10 ± 0.11
2034	35.99	4848 ± 96	1.79 ± 0.25	-1.25 ± 0.15	0.29 ± 0.04	2.781 ± 0.183	2.256 ± 0.167	5.037 ± 0.248	-1.14 ± 0.13
2038	55.53	5277 ± 57	2.56 ± 0.14	-1.36 ± 0.07	0.27 ± 0.02	2.278 ± 0.152	1.607 ± 0.138	3.885 ± 0.205	-1.51 ± 0.10
2055	52.87	4690 ± 40	1.98 ± 0.14	-0.83 ± 0.07	0.28 ± 0.03	3.165 ± 0.132	2.521 ± 0.121	5.687 ± 0.179	-1.02 ± 0.11
2062	36.72	5252 ± 42	2.69 ± 0.12	-0.95 ± 0.06	0.22 ± 0.02	2.671 ± 0.156	2.060 ± 0.139	4.731 ± 0.209	-0.83 ± 0.13
2332	37.09	5190 ± 136	1.92 ± 0.17	-1.52 ± 0.10	0.32 ± 0.03	2.542 ± 0.145	2.512 ± 0.165	5.054 ± 0.220	-0.93 ± 0.13
2355	58.71	4854 ± 86	1.92 ± 0.28	-1.50 ± 0.18	0.24 ± 0.04	2.329 ± 0.145	1.886 ± 0.130	4.215 ± 0.195	-1.51 ± 0.09
2518	39.85	5290 ± 56	2.55 ± 0.14	-1.41 ± 0.07	0.27 ± 0.02	—	—	—	—
2523	45.03	4810 ± 56	1.75 ± 0.17	-1.53 ± 0.09	0.30 ± 0.03	2.585 ± 0.172	2.110 ± 0.172	4.695 ± 0.244	-0.99 ± 0.14
2525	33.89	4820 ± 134	1.79 ± 0.35	-1.37 ± 0.14	0.26 ± 0.05	2.644 ± 0.143	1.959 ± 0.120	4.603 ± 0.186	-1.33 ± 0.10
2561	50.00	5950 ± 56	2.91 ± 0.11	-1.48 ± 0.07	0.27 ± 0.02	2.508 ± 0.149	2.516 ± 0.179	5.024 ± 0.233	-0.58 ± 0.15
2562	36.49	4922 ± 108	1.95 ± 0.29	-1.22 ± 0.15	0.25 ± 0.04	2.827 ± 0.137	2.258 ± 0.127	5.085 ± 0.186	-0.98 ± 0.11
2573	40.69	5317 ± 38	2.67 ± 0.11	-1.32 ± 0.06	0.26 ± 0.02	—	—	—	—
2575	33.24	5351 ± 42	2.74 ± 0.12	-1.27 ± 0.06	0.26 ± 0.02	2.451 ± 0.214	1.962 ± 0.261	4.413 ± 0.337	-1.11 ± 0.17
2748	46.19	4775 ± 134	1.83 ± 0.34	-1.36 ± 0.15	0.26 ± 0.05	2.800 ± 0.170	2.240 ± 0.201	5.040 ± 0.264	-1.07 ± 0.14
2848	39.52	5335 ± 40	2.78 ± 0.12	-1.12 ± 0.06	0.22 ± 0.02	—	—	—	—
2851	55.62	4652 ± 38	2.10 ± 0.12	-0.75 ± 0.07	0.25 ± 0.02	3.299 ± 0.129	2.523 ± 0.107	5.821 ± 0.168	-0.86 ± 0.11
2903	42.28	4760 ± 55	1.73 ± 0.18	-1.63 ± 0.10	0.30 ± 0.03	2.335 ± 0.132	1.933 ± 0.123	4.267 ± 0.180	-1.21 ± 0.10
2963	53.44	4802 ± 135	1.78 ± 0.35	-1.23 ± 0.15	0.26 ± 0.05	2.850 ± 0.113	2.142 ± 0.102	4.992 ± 0.152	-1.04 ± 0.09
2968	62.98	5318 ± 40	2.70 ± 0.12	-1.00 ± 0.05	0.24 ± 0.02	2.539 ± 0.114	2.052 ± 0.103	4.590 ± 0.154	-1.16 ± 0.09
3042	29.55	4926 ± 86	1.96 ± 0.27	-1.50 ± 0.19	0.25 ± 0.04	2.584 ± 0.174	2.113 ± 0.177	4.697 ± 0.248	-0.91 ± 0.14
3068	44.04	4716 ± 38	2.10 ± 0.12	-0.73 ± 0.06	0.27 ± 0.03	3.216 ± 0.143	2.584 ± 0.132	5.800 ± 0.194	-0.82 ± 0.12
3088	40.64	4887 ± 86	1.93 ± 0.28	-1.50 ± 0.19	0.25 ± 0.04	2.437 ± 0.172	1.977 ± 0.161	4.414 ± 0.235	-1.23 ± 0.12
3104	43.91	4927 ± 75	1.91 ± 0.24	-1.64 ± 0.15	0.29 ± 0.05	2.212 ± 0.150	1.802 ± 0.148	4.014 ± 0.211	-1.50 ± 0.10
3162	73.13	4016 ± 34	1.47 ± 0.17	-0.9 ± 0.12	0.28 ± 0.04	3.385 ± 0.099	2.663 ± 0.085	6.048 ± 0.131	-1.22 ± 0.08
3187	42.36	4646 ± 44	1.95 ± 0.14	-0.79 ± 0.07	0.29 ± 0.03	3.203 ± 0.132	2.506 ± 0.109	5.709 ± 0.172	-1.13 ± 0.10
3194	51.23	4040 ± 34	1.61 ± 0.18	-0.92 ± 0.12	0.29 ± 0.04	3.356 ± 0.101	2.582 ± 0.088	5.938 ± 0.134	-1.22 ± 0.08